

# Lift enhancement on spanwise oscillating flat-plates in low-Reynolds-number flows

Shizhao Wang, Guowei He, and Xing Zhang

Citation: Physics of Fluids 27, 061901 (2015); doi: 10.1063/1.4922236

View online: http://dx.doi.org/10.1063/1.4922236

View Table of Contents: http://scitation.aip.org/content/aip/journal/pof2/27/6?ver=pdfcov

Published by the AIP Publishing

# Articles you may be interested in

Onset of unsteady flow in wavy walled channels at low Reynolds number

Phys. Fluids 26, 084104 (2014); 10.1063/1.4892345

A lift formula applied to low-Reynolds-number unsteady flows

Phys. Fluids 25, 093605 (2013); 10.1063/1.4821520

Lift evaluation of a two-dimensional pitching flat plate

Phys. Fluids 25, 091901 (2013); 10.1063/1.4819878

Flow past a normal flat plate undergoing inline oscillations

Phys. Fluids 24, 093603 (2012); 10.1063/1.4749803

Numerical investigations of lift suppression by feedback rotary oscillation of circular cylinder at low Reynolds number

Phys. Fluids 23, 033601 (2011); 10.1063/1.3560379

Did your publisher get

18 MILLION DOWNLOADS in 2014?

AIP Publishing did.



THERE'S POWER IN NUMBERS. Reach the world with AIP Publishing.





# Lift enhancement on spanwise oscillating flat-plates in low-Reynolds-number flows

Shizhao Wang, Guowei He, and Xing Zhang<sup>a)</sup>
The State Key Laboratory of Nonlinear Mechanics (LNM), Institute of Mechanics, Chinese Academy of Sciences, Beijing 100190, China

(Received 18 December 2014; accepted 27 May 2015; published online 11 June 2015)

Numerical simulations are performed to study the influence of spanwise oscillations on the three-dimensional flows around low-aspect-ratio flat-plates at a low Reynolds number of 300. The harmonic spanwise oscillations of the plate are controlled by two parameters: the reduced frequency k and the dimensionless amplitude  $A_y$ . It is found that in a certain range of the parameter space  $(k, A_y)$ , spanwise oscillations are effective in enhancing the average lift and augmenting the average lift-to-drag ratio. To elucidate the mechanism of lift enhancement due to the spanwise oscillations, the wake structures behind flat-plates with and without spanwise oscillations are compared. It is observed that the spanwise oscillation stabilizes the leading-edge vortex and presses it to a place very close to the upper surface. Since a leadingedge vortex corresponds to a low-pressure core, the stably attached leading-edge vortex benefits lift production. This lift-enhancement mechanism is also verified by using a simplified lift formula which links the lift force with the Lamb vector term. The imposed spanwise oscillation is found to enhance the vorticity transport along the spanwise direction, which in turn improves the stability of the leadingedge vortex. The results of this study provide new insight into the counterintuitive high-lift in the gliding flights of tree snakes. © 2015 AIP Publishing LLC. [http://dx.doi.org/10.1063/1.4922236]

#### I. INTRODUCTION

The three types of wing motion most commonly seen in natural and manmade flyer are forward translation (of fixed-wings), flapping, and rotation. The lift generation in the fixed-wing flights (as those of powered airplanes or gliding birds) and some rotating-wing flights (as those of helicopters) can be rationalized by using the steady aerodynamic theory. In this theory, the flow is assumed to be attached to the wing surface and the lift production can be linked with the bounded circulation. For the flapping flights of some animals (such as insects and birds), the unsteady aerodynamic theory is needed to explain the high-lift generated. The essential part of the unsteady aerodynamic theory is the lift generation mechanism associated with the formation of leading-edge vortices (LEVs). Since a LEV corresponds to a low-pressure core, the presence of LEVs on the upper surface greatly enhances the lift. Recently, it was found that in some rotating-wing flights (such as those of descending plant seeds with autorotation), the LEV has also played an important role in lift generation. Despite the abundant literature on the aerodynamic performance of these three types of wing motions, other forms of kinematics are rarely explored. It was not until recently that more complicated wing motions have attracted the attentions of researchers due to their links with the bio-aerial locomotion of some animals.

One such example is the wing morphing in the flapping flights of bats. Bats are very agile animals and their flights show high maneuverability. Bats use their wings to manipulate the air around them in a very complex fashion. One distinct feature in the kinematics of bats' wings (which

a) Electronic mail: zhangx@lnm.imech.ac.cn

lacks in that of insects' wings) is the spanwise stretching-and-retracting motion.<sup>6–8</sup> In a recent work by Wang *et al.*,<sup>9</sup> a heaving rectangular plate with sinusoidally varying wingspan was used as a simplified model for the bats' flapping wings. They found that besides the area effect (an increased wing area during downstroke and a decreased area during upstroke), which apparently enhanced the lift, the spanwise motion may also augment lift by altering the vortical structures.<sup>9</sup>

Another example is the unique kinematics in the gliding flights of paradise tree snakes (*Chrysopelea paradisi*). <sup>10,11</sup> This animal has a superb gliding capability, with a best-recorded gliding angle of 13°. Recently, some wind-tunnel experiments have been conducted to uncover the mystery of high-lift generation in the flying snakes. <sup>12,13</sup> It was found that the counter-intuitively high lift coefficients observed were attributable to the suction by the vortices on the dorsal side of the airfoil which has a snake-like cross-sectional shape. In a subsequent computational study, the enhanced lift was linked with the fact that the primary dorsal vortices were induced to remain close to the surface as a consequence of the interaction between the separated shear layer and the secondary vorticity. <sup>14</sup> Although this study has shed some new light on the cause of the high-lift in flying snakes, only two-dimensional effects of the cross-sectional shape were considered, whereas the three-dimensional S-shaped body and the side-by-side aerial undulations were not included in the simulations.

Inspired by the studies on gliding flights of snakes<sup>14</sup> and the simplified model for bats' flapping flights, in this work, we propose to study the aerodynamic performance of flat-plates in forward flights with harmonic spanwise oscillations. The reasons that we think the spanwise oscillation is particularly important and worth of studying are as follows. This type of motion shares some similarities with the kinematics of gliding snakes. In the recent study by Krishnan et al., 14 it was pointed out that the tree snakes may possibly use the side-by-side undulation to stabilize the LEVs for high lift production. Ellington et al. has postulated that the spanwise flow in the vortex core was necessary to stabilize the LEVs. We thus conjectured that the spanwise oscillation induces spanwise flow in the vortex core, which in turn stabilizes the LEV. Despite some similarities between the kinematics studied here and that in Wang et al., there are still some apparent differences. First, the stretching-and-retracting motion in Wang et al. 9 is always accompanied with area variation, whereas the spanwise oscillation in this work does not change the wing area. Second, in Wang et al., the stretching-retracting motion is superimposed onto to a flapping (heaving) plate in forward flight, whereas in the current study, the spanwise oscillation motion is superimposed onto to a fixed plate in forward flight. Here, we stress that the current study is not aimed at accurately reproducing the lift force generated by a real gliding snake. Instead, we aim at providing some insights into the bio-aerial locomotion of tree snakes by studying the effect of spanwise motion on lift enhancement.

The rest of the paper is arranged as follows. In Sec. II, the numerical methodology, code validations, and computational settings are described. In Sec. III, the simulation results are presented and discussed. Section III A focuses on the effects of spanwise oscillations on the aerodynamic performance. In Sec. III B, the power efficiency in spanwise oscillating plates is addressed. In Sec. III C, the high-lift mechanisms associated with the vortex structures are discussed. Finally, some conclusions are drawn in Sec. IV.

# II. NUMERICAL METHODOLOGY AND SIMULATION SETUPS

#### A. Governing equation and numerical method

The incompressible Navier-Stokes equations are written in a dimensionless form as

$$\frac{\partial \mathbf{u}}{\partial t} + \mathbf{u} \cdot \nabla \mathbf{u} = -\nabla p + \frac{1}{\text{Re}} \nabla^2 \mathbf{u} + \mathbf{f}, \tag{1}$$

$$\nabla \cdot \mathbf{u} = 0, \tag{2}$$

where  $\mathbf{u}$  is the velocity vector, p is the pressure, and Re is the Reynolds number.  $\mathbf{f}$  is the Eulerian force density that is used to mimic the effect of the immersed body on the flow. Here, the Reynolds

number is defined as  $Re = U_{\infty}c/\nu$ , where  $U_{\infty}$ , c, and  $\nu$  are the oncoming flow velocity, the chord length of the flat-plate, and the kinematic viscosity of the fluid, respectively.

We use a direct-forcing immersed boundary method which is based on the discrete stream-function formulation  $^{15}$  to solve the Navier-Stokes equations. We attempt to model an infinitely thin flat-plate by using a series of Lagrangian (marker) points where the Lagrangian force density  $\mathbf{F}(\mathbf{X},t)$  is defined. The forcing term at the Eulerian points and that at the Lagrangian points are related by

$$\mathbf{f}(\mathbf{x},t) = \int_{S} \mathbf{F}(\mathbf{X},t)\delta(\mathbf{x} - \mathbf{X})dS,$$
(3)

where S is the control surface area in the Lagrangian coordinate system and  $\delta$  is the regularized delta-function. To mimic the effect of the immersed body on the fluid, the "no-slip" condition is imposed at the Lagrangian points, i.e.,

$$\int_{V} \mathbf{u}(\mathbf{x}, t) \delta(\mathbf{x} - \mathbf{X}) dV = \mathbf{U}_{b}(\mathbf{X}, t), \tag{4}$$

where  $U_b$  is the velocity of the Lagrangian point, which can be determined by the prescribed kinematics of the plate. Unlike the sharp-interface immersed boundary method <sup>16</sup> (where the velocity reconstruction is needed), for the diffusive-interface-type immersed method in the present study, no special difficulty is encountered in handling an infinitely thin surface.

Equation (4) serves as the constraint condition which is used to determine the Lagrangian forcing  $\mathbf{F}(\mathbf{X},t)$ . After obtaining  $\mathbf{F}(\mathbf{X},t)$ , the Eulerian forcing  $\mathbf{f}(\mathbf{x},t)$  can be computed by using Eq. (3). For the detailed descriptions of the immersed boundary method, please refer to the paper by Wang and Zhang. The issues regarding the parallel implementation of the immersed boundary method can be found in the work by Wang *et al.* <sup>17</sup>

The geometry of the flat-plate is defined by its span b and chord length c (with an aspect ratio of AR = b/c). The angle of attack  $\alpha$  is defined as the angle between the chord line and the oncoming flow. The flat-plate undergoes spanwise oscillatory motions (see Figure 1), in which the y coordinate of the centre of the plate is prescribed in a dimensionless form as

$$Y(t) = A_u \cos(2kt). (5)$$

Here, k is the reduced frequency which is defined as  $k = \pi f c/U_{\infty}$ , where f is the (dimensional) oscillation frequency.  $A_y$  is the dimensionless oscillation amplitude. t is the dimensionless time. The reference length and time used in the scaling are c and  $c/U_{\infty}$ , respectively.

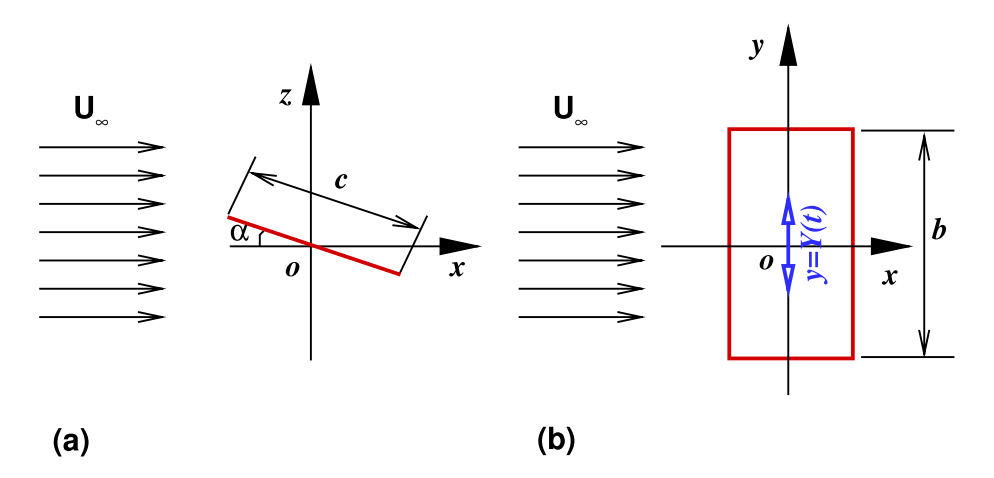


FIG. 1. Schematic depiction of flow over a flat-plate with spanwise oscillations: (a) side view and (b) top view.

The coefficients of aerodynamic forces are calculated by

$$C_{d} = \frac{-\sum_{n=1}^{M} F_{x}(\mathbf{X}_{n}, t) \Delta s}{\frac{1}{2} \rho U_{\infty}^{2} A},$$

$$C_{l} = \frac{-\sum_{n=1}^{M} F_{z}(\mathbf{X}_{n}, t) \Delta s}{\frac{1}{2} \rho U_{\infty}^{2} A},$$

$$C_{s} = \frac{-\sum_{n=1}^{M} F_{y}(\mathbf{X}_{n}, t) \Delta s}{\frac{1}{2} \rho U_{\infty}^{2} A},$$

$$(6)$$

where  $\rho$  is the density of the fluid, and A is the surface area of the plate.  $\Delta s$  is the surface area of the marker element in the Lagrangian coordinate system.  $F_x$ ,  $F_z$ , and  $F_y$  denote the Lagrangian force components in the horizontal, vertical, and lateral directions, respectively.

In the present study, the aerodynamic performance of the flat-plates is quantified using the average force coefficients which are computed by

$$\overline{C}_{d,l,s} = \frac{1}{T} \int_{t}^{t+T} C_{d,l,s}(t)dt.$$
 (7)

In the case of oscillating plate, T equals the period of the prescribed spanwise oscillation. In the case of non-oscillating plate, due to the possible presence of aperiodic flows, <sup>18</sup> a much longer averaging time (T = 100) is used.

# B. Code validations and simulation setups

The code used in this study has been validated previously by using the flows past a stationary flat-plate of AR = 2 at Re = 100. The results of the tests indicated that for a wide range of angle of attack  $\alpha$ , the lift and drag coefficients are in agreement with those from the references. <sup>15</sup>

To further test its capability of handling moving boundaries, the flow around a flapping wing is simulated. The simulation setups are the same as those of Shyy *et al.*, <sup>19</sup> in which the aerodynamics of a hovering flapping flat-plate experiencing no freestream was studied. The kinematics of the flat-plate is prescribed as

$$X(t) = h_a \sin(2\pi f t), \quad \alpha(t) = \alpha_0 - \alpha_a \sin(2\pi f t + \phi), \tag{8}$$

where X(t) is the time dependent plunging position,  $h_a$  the plunging amplitude, f the plunging (or) pitching frequency,  $\alpha(t)$  the time dependent pitching angle,  $\alpha_0$  the time-averaged pitching angle,  $\alpha_0$ 

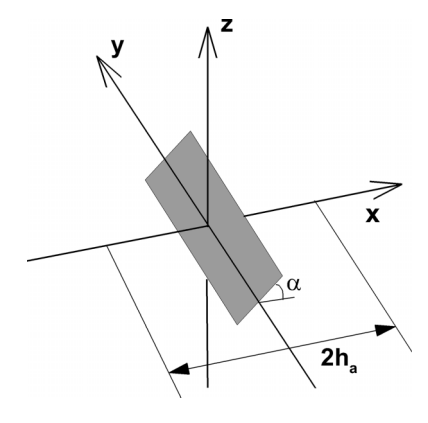


FIG. 2. Schematic depiction of the problem: a hovering flapping flat-plate.

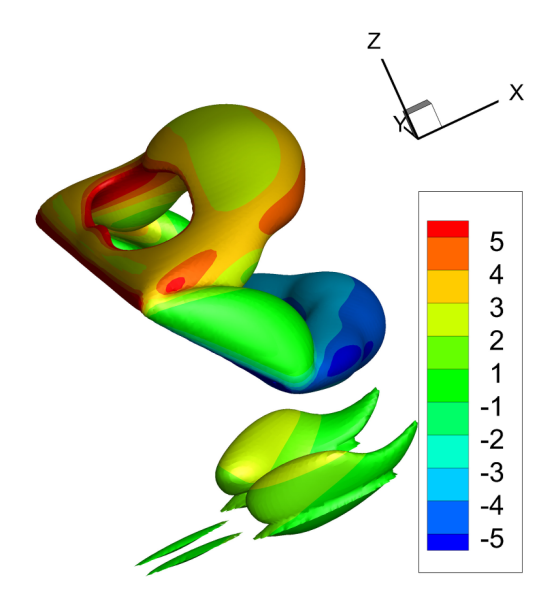


FIG. 3. Flow structures around the flapping flat-plate. The flow structures are identified by using the Q-criterion and the iso-surfaces for Q = 1.0 are shown. The colors represent the values of spanwise vorticity.

the angular amplitude of pitching, and  $\phi$  the phase difference between the plunging and pitching (see Figure 2).

The aspect ratio of the flat-plate is AR = b/c = 4. The Reynolds number based on the maximum plunging velocity  $U_{max}$ , chord length c, and kinematic viscosity of the fluid v is  $Re = U_{max}c/v = 100$ . The reduced frequency, as defined in the work of Shyy  $et\ al.$ ,  $ext{19}$  is  $ext{19}$  is  $ext{10}$  is  $ext{10}$ . The other parameters are  $ext{10}$  and  $ext{10}$  in  $ext{10}$  and  $ext{10}$  is  $ext{10}$ . The computational domain is  $ext{10}$  is  $ext{10}$ . The mesh is locally refined in a domain of  $ext{10}$ , with non-slip boundary condition on all the boundaries. The mesh is locally refined in a domain of  $ext{10}$ ,  $ext{10}$ ,  $ext{10}$ ,  $ext{10}$ , with a grid length of 0.025. The time step is chosen by setting the Courant–Friedrichs–Lewy (CFL) number to 0.5. The flow structures around the wing are shown in Figure 3. The time history of lift coefficient agrees very well with that of Shyy  $ext{10}$  as shown in Figure 4.

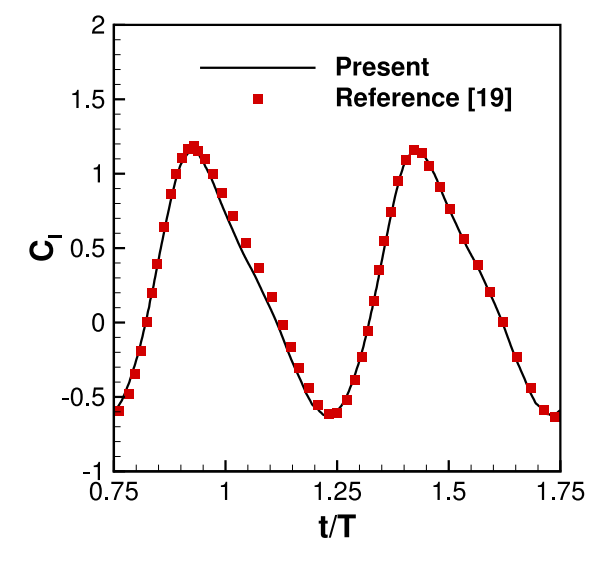


FIG. 4. The time history of lift coefficient for a hovering flapping flat-plate. Here, the lift coefficient is computed by using  $U_{max}$  as the reference velocity. The squares denote the results from the paper by Shyy *et al.*<sup>19</sup>

	25	35	45
	(deg)	(deg)	(deg)
$\overline{\overline{C}_l}$ (original mesh)	1.25	1.54	1.48
$\overline{C}_l$ (finer mesh)	1.25	1.54	1.48
$\overline{C}_l$ (larger domain)	1.25	1.54	1.48
$\overline{C}_d$ (original mesh)	0.74	1.12	1.50
$\overline{C}_d$ (finer mesh)	0.75	1.12	1.50
$\overline{C}_d$ (larger domain)	0.74	1.12	1.49

TABLE I. Dependency of lift and drag coefficients on mesh resolution and domain size for the case of  $A_y = 1.0$  and k = 0.5.

In the study of flat-plates with spanwise oscillations, simulations are performed on a rectangular cube ( $[-6,12] \times [-9,9] \times [-9,9]$ ), with the minimum grid width being 0.025 and the maximum grid width being 0.2. Grid stretching is applied in all the three directions with finer resolution near the flat-plate in order to capture the wake structures. Please note that in the region near the flat-plate, uniform mesh cells are used to ensure good accuracy in performing the interpolations of Eqs. (3) and (4).

The boundary conditions on the six sides of the cube are as follows. At the inlet, a uniform velocity (1,0,0) is prescribed. At the four side-walls, the normal velocity component is zero and a zero-gradient condition is applied to the tangential velocity component. At the outlet, a zero-gradient condition is applied to the tangential velocity component. The normal velocity component at the outlet is computed from the stream functions, which are treated as unknowns (as those in the interior). This boundary condition is equivalent to the constant-pressure condition for flow solvers which use the primary-variable formulation.

The initial condition for the fluid velocity is (1,0,0). At  $t = 0^+$ , the non-slip boundary condition is suddenly imposed on the Lagrangian points. The time steps in the simulation are chosen such that the maximum *CFL* number never exceeds 0.5. In this study, we are only interested in the long-time behavior of the flows. Thus before the average aerodynamic forces are evaluated, we run the code for a long time (more than 10 oscillation cycles in the case of oscillating plates) for the starting procedure to lose its effects on the flows.

To test the effects of domain size and mesh resolution on the results, additional simulations are performed on a finer mesh and also on a larger computational domain. More specifically speaking, for the case of AR = 2 and Re = 300, with a spanwise oscillation of  $A_y$  = 1.0 and k = 0.5, we generate a finer mesh on the original computational domain, with a minimum grid width of 0.0125. We also attempt to use a larger computational domain of the size [-12,18] × [-15,15] × [-15,15] while keeping the mesh resolution unchanged. The average lift and drag coefficients at three different angles of attack are listed in Table I. It is seen that the results obtained are almost indistinguishable. For other simulations performed in this study, similar checks are also conducted to ensure that the results are independent of the mesh resolution and the domain size.

#### III. RESULTS AND DISCUSSIONS

A summary of the simulations performed in this study is presented in Table II. Seven series of cases (A-G) are simulated. In all cases, the Reynolds number is set to 300 (except for series E). For series A, B, C, D, and E, the aspect ratio is set to 2.0 and six angles of attack ranging from 10° to 60° are considered. For series A, three reduced frequencies are considered with the dimensionless amplitude being fixed to 1.0. For series B, two dimensionless amplitudes are considered with the reduced frequency being fixed to 0.5. For series C, the dimensionless amplitude and the reduced frequency are 1.0 and 0.5, respectively. For series D and E, simulations are performed on a flat-plate in purely forward flight at the Reynolds number of 300 and 500, respectively. For series F and G, flat-plates with the aspect ratios of 1.0 and 3.0 are considered,

Case	Re	AR	$\alpha$ (deg)	k	$A_y$
A	300	2	10, 15, 25, 35, 45, 60	0.25, 0.5, 1.0	1.0
В	300	2	10, 15, 25, 35, 45, 60	0.5	0.25, 0.5
C	300	2	10, 15, 25, 35, 45, 60	1.0	0.5
D	300	2	10, 15, 25, 35, 45, 60	•••	0
E	500	2	10, 15, 25, 35, 45, 60		0
F	300	1, 3	25	0.25	1.0
G	300	1, 3	25	•••	0

with the angle of attack being fixed to 25°. For series F, the reduced frequency and dimensionless amplitude are set to 0.25 and 1.0, respectively. For series G, a flat-plate in purely forward flight is considered.

In the numerical simulations of this work, the angle of attack is between  $10^{\circ}$  and  $60^{\circ}$ , while the oscillation Strouhal number,  $2kA_y/\pi$ , lies in the range of 0.06–0.6. According to Krishnan *et al.*<sup>14</sup> and Socha *et al.*,<sup>20</sup> the angle of attack for the anterior body of a gliding snake lies in the range of  $20^{\circ}$ – $40^{\circ}$ , while the oscillation Strouhal number in real gliding snakes is around 0.06. Thus, the parameter values used in the current work are in the reasonable range.

The gliding flights of tree snakes occur at the Re numbers of 5000–15000. In the present work, we focus on cases with a much lower Reynolds number of 300. Some explanations regarding the Reynolds number difference in these two scenarios are presented as below. First, a thorough parametric study on cases (especially three-dimensional ones) with a Reynolds number as high as 10<sup>4</sup> is still beyond the limits of our computing capability. Usually, in numerical studies of bio-locomotion problems, the Re numbers considered are much lower than those in the real-world situations. For example, in the two-dimensional study of flow over a "snake-body-like" cross section, 14 the Re number was in the range of 500-3000 (which was reduced by one order in magnitude if compared with those of gliding snakes). In the study of flapping plate with a stretching-retracting motion, the Re number was set to 300 (whereas the Re numbers for bats' flights lie in the range of  $10^3-10^5$ ). Second, as that pointed out by Wang et al., within the scope of fast laminar flows and under certain circumstances, the large-scale flow structures which are responsible for the high-lift generation are not very sensitive to the Re number. In the present work, the geometry shape considered is a rectangular plate with a sharp leading edge. This geometry can cause flow separations immediately at the leading edge (the separation point is not sensitive to the Re number). Furthermore, if the imposed wing motion (such as the spanwise oscillation of this work) is strong enough compared with the oncoming flow, the flow structure is largely dependent on the prescribed motion and is also insensitive to the Re number. Some supporting evidences have been provided by Viswanath et al., where the kinematics of bat's flapping wing was measured and used as the inputs to a flow solver to evaluate the aerodynamic performance of bat's climbing flight. The aerodynamic forces, the formation, evolution, and phasing of the unsteady flow structure were found to be insensitive to the Re number. Similar conclusions regarding the Reynolds number effect can also be found in some other references. 21,22 Although a much lower Re number is considered in the present work, we believe that the main flow structures which are responsible for the lift production are not sensitive to Re number. Thus, the results of this study can still shed light on the counterintuitive high-lift in the gliding flights of tree snakes.

In this work, we focus on a wing with the simplest cross-sectional shape, i.e., a thin flat-plate. As a matter of fact, the cross-sectional shape can affect the location of separation point, which in turn varies the lift and drag. For the flat-plate, flow separation always occurs at the sharp edge and this location is independent of the *Re* number. For wings with smooth curved surfaces, the location of separation point strongly depends on both the cross-sectional shape and the *Re* number. Despite the fact that the lift and drag are dependent on the cross-sectional shape, it is expected that the effect of spanwise oscillation in enhancing lift is universal (please see Sec. III C for the discussion on lift-enhancement mechanism associated with spanwise oscillation).

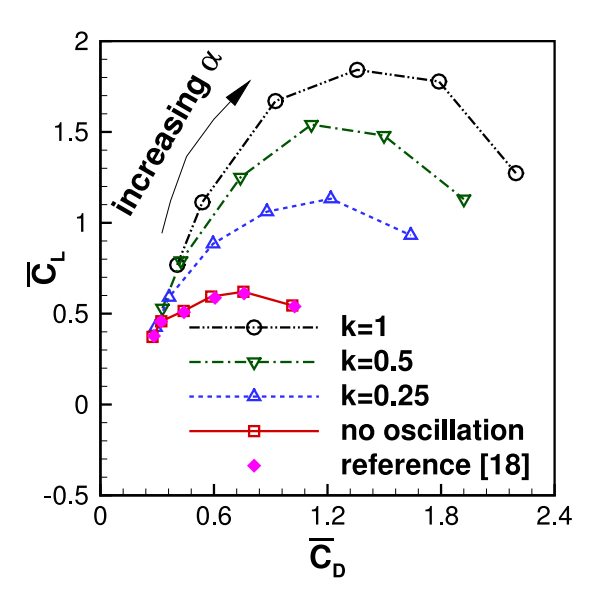


FIG. 5. Drag polar graph for flat-plates (AR = 2, Re = 300) with no oscillation and oscillations of three different reduced frequencies. Six angles of attack ( $10^{\circ}$ ,  $15^{\circ}$ ,  $25^{\circ}$ ,  $35^{\circ}$ ,  $45^{\circ}$ , and  $60^{\circ}$ ) are considered. For all oscillating cases,  $A_y = 1.0$ . The results for the non-oscillating case from Taira and Colonius<sup>18</sup> are also plotted for comparison.

## A. Average aerodynamic forces

We now look at three important quantities for accessing the aerodynamic performance, namely, the average lift coefficient, the average drag coefficient, and the average lift-to-drag ratio.

First, we study the effect of reduced frequency k on the average lift and drag coefficients. The drag polar for various reduced frequencies at a fixed dimensionless amplitude of  $A_y = 1.0$  (series A in Table II) is shown in Figure 5. From this figure, we can see that when the spanwise oscillations are imposed, the average lift and drag coefficients become much larger (compared with the non-oscillating case). For a fixed dimensionless amplitude and angle of attack, both the lift and the drag coefficients increase monotonically with increasing k. In a flat-plate without spanwise oscillations, the maximum lift coefficient (among all angles of attack) is around 0.6. The maximum lift coefficients increase by a factor of 1.8, 2.5, and 3.0 for k = 0.25, 0.5, and 1.0, respectively.

Figure 6 shows the lift-to-drag ratio as a function of angle of attack for various reduced frequencies at a fixed dimensionless amplitude of  $A_y=1.0$ . It is seen that the maximum lift-to-drag ratio is always achieved near  $\alpha=15^\circ$  for flat-plates with or without spanwise oscillations. In a flat-plate without spanwise oscillations, the maximum lift-to-drag ratio is around 1.4. The maximum lift-to-drag ratios increase by a factor of 1.14, 1.32, and 1.46 for k=0.25, 0.5, and 1.0, respectively. At small angles of attack, the lift-to-drag ratios increase monotonically with increasing k. At large angles of attack ( $\alpha \ge 35^\circ$ ), however, the lift-to-drag ratios first increase and then saturate with increasing k.

Next, we study the effect of dimensionless amplitude on the aerodynamic performance by varying  $A_y$  while keeping k fixed. Figure 7 shows the drag polar for various dimensionless amplitudes at k=0.5. It is seen that the trends in the average lift and drag coefficients with increasing  $A_y$  are very similar to those with increasing k at a fixed  $A_y$  (see Figure 5). Compared with that obtained in the non-oscillating case, the maximum lift coefficients increase by a factor of 1.3, 1.8, and 2.5 for  $A_y=0.25, 0.5,$  and 1.0, respectively.

Figure 8 shows the lift-to-drag ratio as a function of angle of attack for various dimensionless amplitudes at a fixed reduced frequency of k = 0.5. Comparing with that obtained in the non-oscillating case, the maximum lift-to-drag ratios increase by a factor of 1.07, 1.18, and 1.32 for  $A_y = 0.25$ , 0.5, and 1.0, respectively. For a wide range of angle of attack, the lift-to-drag ratios increase monotonically with increasing  $A_y$ . The saturation of the lift-to-drag ratio with increasing  $A_y$  is only observed at very large angles of attack ( $\alpha > 60^{\circ}$ ).

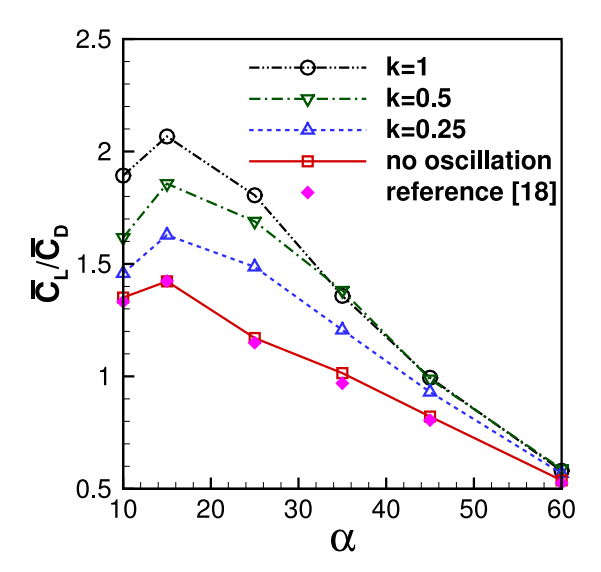


FIG. 6. Average lift-to-drag ratio as a function of angle of attack for flat-plates (AR = 2, Re = 300) with no oscillation and oscillations of three different reduced frequencies. Six angles of attack ( $10^{\circ}$ ,  $15^{\circ}$ ,  $25^{\circ}$ ,  $35^{\circ}$ ,  $45^{\circ}$ , and  $60^{\circ}$ ) are considered. For all oscillating cases,  $A_y = 1.0$ . The results for the non-oscillating case from Taira and Colonius  $^{18}$  are also plotted for comparison.

From Figures 5 and 7, it is seen that the lift enhancement due to oscillation is not significant at low angle of attack. This is because the major effect of spanwise oscillation is to stabilize the LEVs on the upper surface and thus enhance lift. At low angles of attack, the LEVs are too weak (or not formed at all); thus the spanwise oscillation can barely affect the lift production.

From Figures 6 and 8, it is seen that at large angles of attack, the lift-to-drag will saturate as  $A_y$  (or k) of the oscillation increases. The explanation on the cause of this phenomenon is as follows. At large angles of attack, due to the existence of large scale separation, the pressure force dominates the total force exerted on the plate. The spanwise oscillation may increase the magnitudes of both lift and drag, but the pressure force still dominates the total force. Since the direction of the pressure force is always perpendicular to the surface, the lift-to-drag ratio can be approximated by  $(\tan \alpha)^{-1}$ .

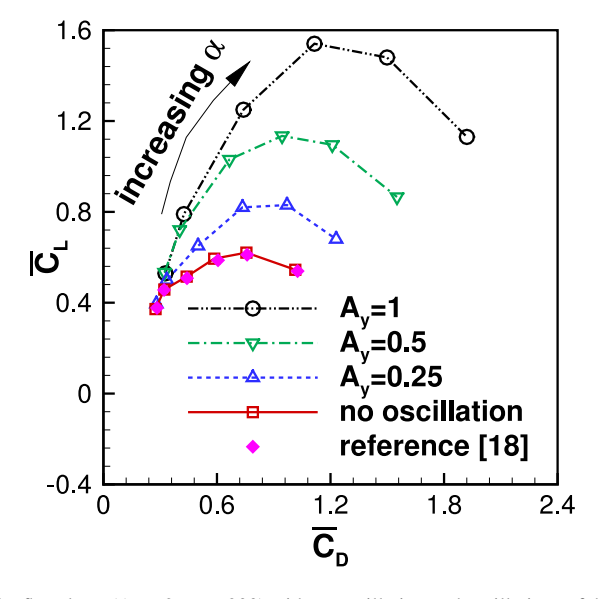


FIG. 7. Drag polar graph for flat-plates (AR = 2, Re = 300) with no oscillation and oscillations of three different dimensionless amplitudes. Six angles of attack ( $10^\circ$ ,  $15^\circ$ ,  $25^\circ$ ,  $35^\circ$ ,  $45^\circ$ , and  $60^\circ$ ) are considered. For all oscillating cases, k = 0.5. The results for the non-oscillating case from Taira and Colonius<sup>18</sup> are also plotted for comparison.

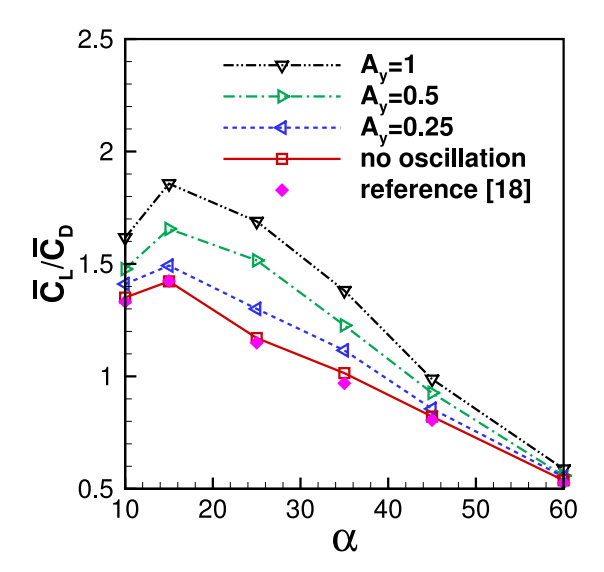


FIG. 8. Average lift-to-drag ratio as a function of angle of attack for flat-plates (AR = 2, Re = 300) with no oscillation and oscillations of three different dimensionless amplitudes. Six angles of attack ( $10^{\circ}$ ,  $15^{\circ}$ ,  $25^{\circ}$ ,  $35^{\circ}$ ,  $45^{\circ}$ , and  $60^{\circ}$ ) are considered. For all oscillating cases, k = 0.5. The results for the non-oscillating case from Taira and Colonius are also plotted for comparison.

Thus, we can see that the lift-to-drag ratio is a function of angle of attack  $\alpha$  only and is *independent* of the strength of the spanwise oscillation (magnitudes of  $A_y$  and k).

The effect of oscillating Strouhal number  $2kA_y/\pi$  (which represents the ratio of the spanwise velocity over the forward velocity) on the aerodynamic performance is also studied here. We compare the drag polar plots for different combinations of  $A_y$  and k, but with a fixed value of  $A_yk$ . Figure 9 shows the drag polar plots for four cases: (1)  $k = 0.25, A_y = 1.0$ ; (2)  $k = 0.5, A_y = 0.5$ ; (3)  $k = 0.5, A_y = 1.0$ ; and (4)  $k = 1.0, A_y = 0.5$ . From this figure, it is seen that the two curves with  $A_yk = 0.25$  are very close to each other, although not identical. However, the two curves with  $A_yk = 0.5$  are very different. Thus, we can see that the aerodynamic performance of an oscillating plate does not solely depend on the oscillating Strouhal number (but rather on  $A_y$  and k

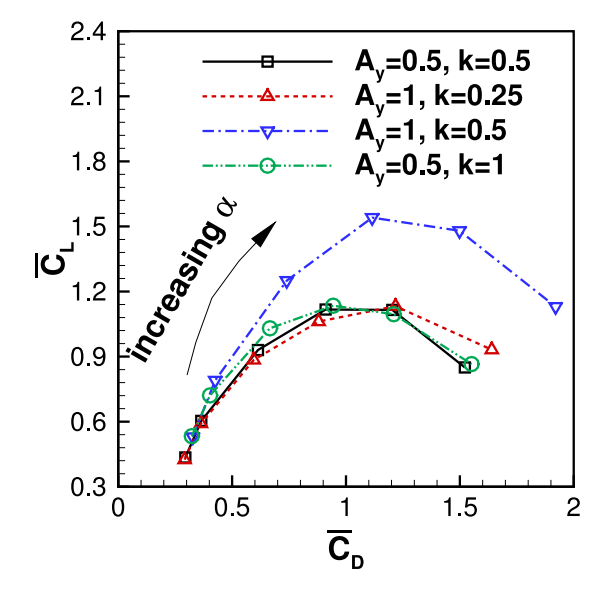


FIG. 9. Drag polar graph for the flat-plates (AR = 2, Re = 300) with four combinations of oscillation frequencies and amplitudes. Six angles of attack ( $10^{\circ}$ ,  $15^{\circ}$ ,  $25^{\circ}$ ,  $35^{\circ}$ ,  $45^{\circ}$ , and  $60^{\circ}$ ) are considered.

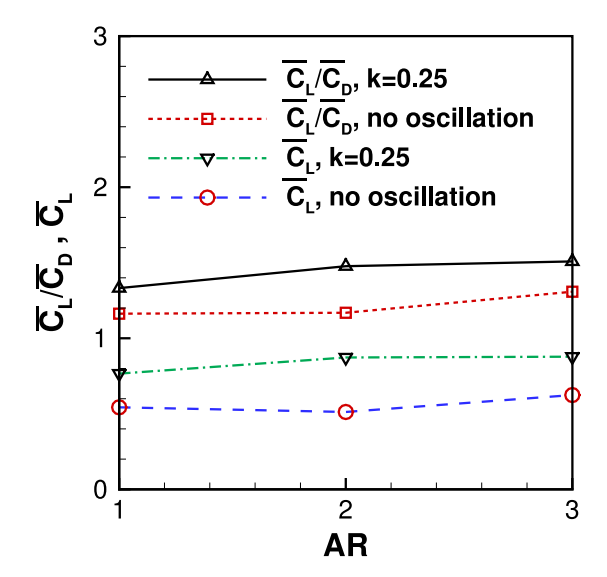


FIG. 10. Average lift coefficient and lift-to-drag ratio as functions of aspect ratio for flat-plates of Re = 300 and  $\alpha = 25^{\circ}$ . Both the non-oscillating cases and the oscillating cases with k = 0.25 and  $A_{y} = 1.0$  are plotted.

individually). If  $A_y k$  remains fixed, the overall trend of the performance is that "lower frequency with larger amplitude" is better than "higher frequency with smaller amplitude."

The influence of aspect ratio on the aerodynamic performance is studied by varying AR while keeping other parameters fixed (Re = 300, k = 0.25,  $A_y$  = 1.0, and  $\alpha$  = 25°). Figure 10 shows the average lift and average lift-to-drag ratio as functions of AR. It is seen that for three different aspect ratios (1.0, 2.0, and 3.0), the variations in the average lift and lift-to-drag ratio never exceed 15%. Thus, the average lift and average lift-to-drag ratio are not very sensitive to the aspect ratio of the plate (at least in the range of  $1 \le AR \le 3$ ) for flat-plates with and without spanwise oscillations.

## B. Power efficiency in spanwise oscillating plates

We now proceed to assess the power efficiency in the spanwise oscillating plates for generating lift. More specifically speaking, we will evaluate the mechanical power consumption subject to the constraint of load balance.<sup>23,24</sup> Here, we consider the inverse of the dimensionless aerodynamic power required to support a given load. The power efficiency (also known as "power factor"<sup>24</sup>) is defined as

$$\eta = \frac{MgU_{ref}}{U_{\infty} \cdot \frac{1}{T} \int_{0}^{T} F_{X}(\tilde{t})d\tilde{t} + \frac{1}{T} \int_{0}^{T} -F_{Z}(\tilde{t}) \cdot Z'(\tilde{t})d\tilde{t}},\tag{9}$$

subject to the constraint

$$\frac{1}{T} \int_0^T F_Y(\tilde{t}) d\tilde{t} = Mg. \tag{10}$$

Here, Mg is the load supported by the flat-plate.  $F_X$ ,  $F_Y$ , and  $F_Z$  are the instantaneous force components in the streamwise, transverse, and spanwise direction, respectively.  $\tilde{t}$  is the *dimensional* time. The reference velocity in Eq. (9) is defined as  $U_{ref} = \sqrt{2Mg/\rho A}$ .

By using the definitions of force coefficients Eq. (6), and substituting Eqs. (7) and (10), Eq. (9) can be reformulated as

$$\eta = \frac{\bar{C}_L^{\frac{3}{2}}}{\bar{C}_D + \left(\frac{2\bar{A}_Z}{\pi}\right) k^2 \int_0^{\frac{\pi}{k}} C_s(t) \sin(2kt) dt},\tag{11}$$

where t is the dimensionless time. For a plate in purely forward flight, a more familiar form of  $\eta = \bar{C}_L^{\frac{3}{2}}/\bar{C}_D$  is recovered.

A rational evaluation of efficiency in lift generation requires the comparison of power factors among cases which support the *same* load. If the *Re* number is fixed, the non-oscillating case may not be able to generate enough lift to support the same load as that of the oscillating cases. Thus, it is not appropriate to make comparisons among various cases of a fixed *Re*. To facilitate a fair comparison, we first defined a modified Reynolds number as

$$Re^* = \frac{U_{ref}c}{v} = \sqrt{\frac{2Mg}{A\rho}} \cdot \left(\frac{c}{v}\right) = (\bar{C}_L)^{1/2}Re.$$
 (12)

In deriving the equation above, we use the definitions of the Reynolds number Re and the reference velocity  $U_{ref}$ , and also the dimensionless form of the constraint of lift-weight balance, i.e.,

$$\frac{1}{2}\rho U_{\infty}^2 A \bar{C}_L = Mg. \tag{13}$$

The modified Reynolds number  $Re^*$  is a *constant* for cases where a given lift force is generated, although the Re number may differ from case to case.

In Figure 11, we plot the power factor against the modified Reynolds number for several cases with and without spanwise oscillations. From this figure, we can conclude that the oscillating plates outperform the plate in purely forward flight, and the best efficiency is achieved in the plate with a moderate frequency (if the oscillating amplitude is fixed). For  $Re^* = 336$ , the optimal power factor is achieved at  $\alpha = 25^\circ$ , by a oscillating plate with k = 0.5 and  $A_y = 1.0$ . This power factor is 1.8 times as large as that achieved in a non-oscillating plate. Please note that the *inertia* power needed for maintaining the oscillatory motion of the plate is not included in the denominator of Eq. (9). Thus, the conclusions above are only valid if the lift-generating plate is very *light* when comparing with the total load supported.

# C. Vortical structures and high-lift mechanism

In this subsection, the lift-enhancement mechanism in a spanwise oscillating plate will be elucidated by dissecting its vortical structures. First, for one typical case of AR = 2, Re = 300,

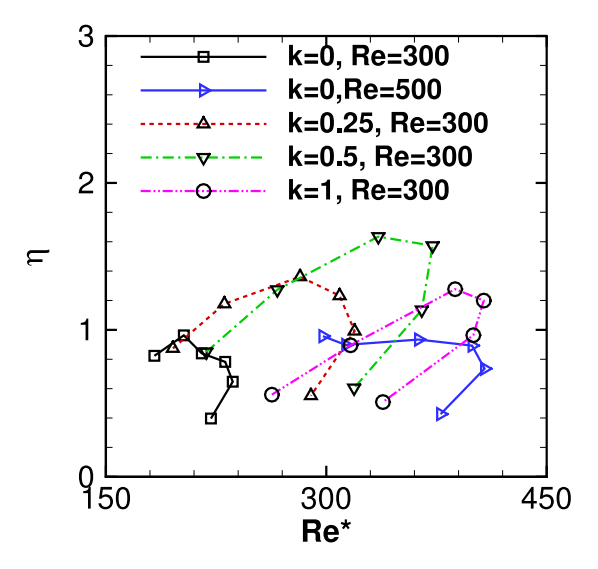


FIG. 11. Power efficiency vs. modified Reynolds number for a non-oscillating plate and plates with a dimensionless oscillation amplitude of 1.0. The aspect ratio of the plates is 2.0. Six angles of attack (10°, 15°, 25°, 35°, 45°, and 60°) are considered.

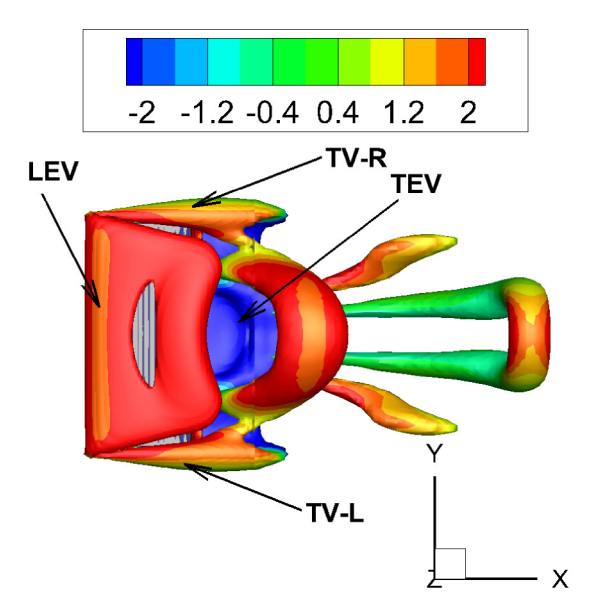


FIG. 12. Visualization of the typical vortex structure (top view) for a flat-plate (AR = 2.0, Re = 300, and  $\alpha = 25^{\circ}$ ) in forward flight without oscillation. The flow structures are identified by using the Q-criterion and the iso-surfaces for Q = 0.75 are shown. The colors represent the values of spanwise vorticity. (Multimedia view) [URL: http://dx.doi.org/10.1063/1.4922236.1]

and  $\alpha = 25^{\circ}$ , we compare the vortical structures around the flat-plates with and without spanwise oscillation.

The typical wake structure behind a flat-plate in forward flight is shown in Figure 12 (multimedia view). The primary vortical structures include a LEV, a trailing-edge vortex (TEV), and a pair of counter-rotating tip vortices (TVs). The LEV and TVs remain as separated vortical structures and are not connected to each other. This is one distinct feature observed in the flows over *rectangular* plates because of the presence of right-angled corners. For other planforms, such as ellipse, semicircle, and delta, these three vortical structures are found to be connected continuously. At this angle of attack, the LEV and TEV roll up and detach from the surface repeatedly. The shedding of these structures results in an unsteady wake characterized by a series of hairpin vortices.

Figure 13 (multimedia view) shows six snapshots of vortical structures throughout one half oscillating cycle behind a flat-plate with the spanwise oscillation of k=0.5 and  $A_y=1.0$ . It is seen that the wake topology is completely altered by the imposed spanwise oscillation. The pair of tip vortices which appear in the non-oscillating case can no longer be seen. Instead, a more compact side-edge vortex (SEV) rolls up alternatively at the two wing-tips. The SEV is initially generated when a wing-tip advances into the fluid. At this moment, the SEV is disconnected with the LEV and the TEV. At the moment when the wing-tip starts to retreat from the fluid, the LEV, the SEV, and the TEV are interconnected to form a complex, elongated vortical structure. Parts of this vortical structure finally pinch off after being further stretched. The shedding of these segments of the elongated structures results in an unsteady wake characterized by a series of vortex "ribbons."

Further analysis indicates that the lift enhancement in the spanwise oscillating plates is primarily attributable to the modulation of the vortical structures. In Figure 14, we plot the distribution of spanwise vorticity on the mid-span slice for both the plates with and without spanwise oscillation. For the purpose of comparison, the distribution of spanwise vorticity on the mid-span slice of a hovering flapping plate (for the validation case presented in Sec. II B) is also shown. For the non-oscillating case (Figure 14(a)), no stably attached LEV is formed. Instead, large-scale separation and vortex shedding are observed. For the plate with spanwise oscillation (Figure 14(b)), it is seen that a LEV stays at a position very closer to the upper surface. Because a LEV corresponds to a low-pressure core, the stably attached LEV is beneficial to the lift production. For the hovering flapping case (Figure 14(c)), we notice that a LEV is able to attach to the foil stably, even at a much larger angle of attack (around 45°). The formation of stable LEVs has long been recognized

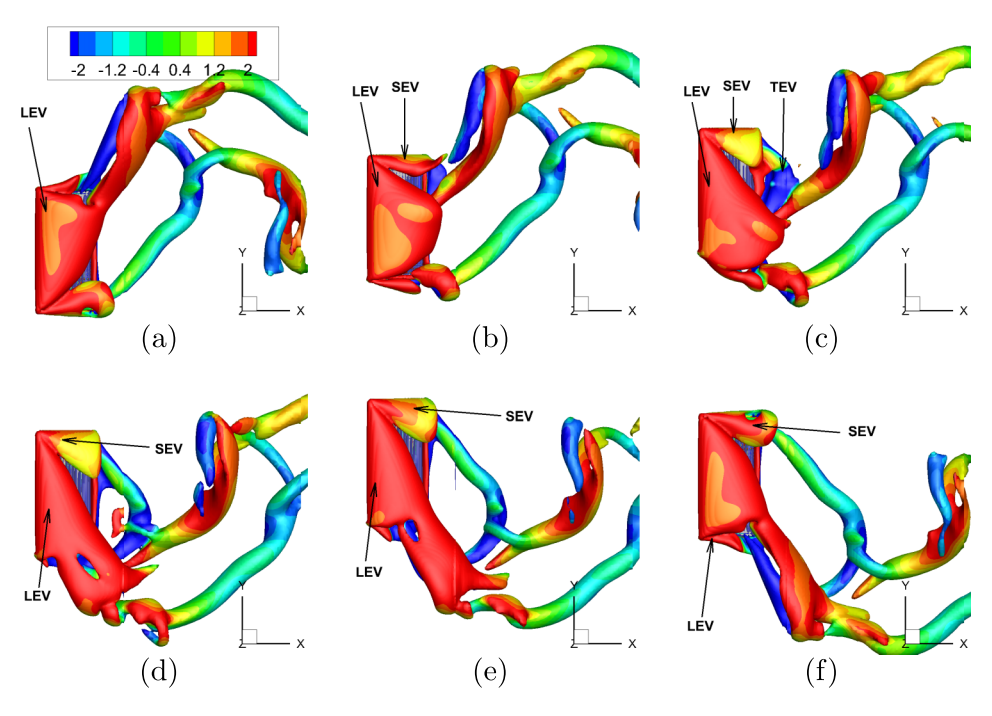


FIG. 13. Visualization of the vortex structures (top view) throughout one half oscillating cycle for a flat-plate (AR = 2.0, Re = 300, and  $\alpha = 25^{\circ}$ ) with the oscillation of k = 0.5 and  $A_y = 1.0$ . (a) t = 0.5T; (b) t = 0.6T; (c) t = 0.7T; (d) t = 0.8T; (e) t = 0.9T; (f) t = 1.0T. The flow structures are identified by using the Q-criterion and the iso-surfaces for Q = 0.75 are shown. The colors represent the values of spanwise vorticity. (Multimedia view) [URL: http://dx.doi.org/10.1063/1.4922236.2]

as the key mechanism for generating high lift in flapping flights of animals. The mechanism for the stabilization of LEVs in spanwise oscillating and flapping foils will be discussed hereinafter.

By using a simplified formula for the approximate decomposition of lift force, <sup>25</sup> we can establish a direct and quantitative relation between the lift enhancement and the modulation of vortical structures. This simplified lift formula reads

$$C_{L} \approx 2\left(\int_{V} (\mathbf{u} \times \omega)_{z} dV - \int_{V} \frac{\partial u_{z}}{\partial t} dV\right)$$

$$= 2 \int_{V} u_{x} \omega_{y} dV - 2 \int_{V} u_{y} \omega_{x} dV - 2 \int_{V} \frac{\partial u_{z}}{\partial t} dV,$$

$$\underbrace{-2 \int_{V} u_{x} \omega_{y} dV}_{Term \ Lamb \ 1} \underbrace{-2 \int_{V} u_{y} \omega_{x} dV}_{Term \ Lamb \ 2} \underbrace{-2 \int_{V} \frac{\partial u_{z}}{\partial t} dV}_{Term \ acc},$$
(14)

where  $\mathbf{u} \times \omega$  is the Lamb vector. The subscripts x, y, and z represent the components of the vector in streamwise, spanwise, and vertical directions, respectively. V is a control volume which encloses the flat-plate. In this work, V is a rectangular cube of the size  $[-4, x_t] \times [-5, 5] \times [-9, 9]$ , where  $x_t$  is the x-position of the trailing-edge. The underlying principles for the choice of control volume in the simplified lift formula can be found in the paper by Wang  $et\ al.^{25}$ 

The Lamb vector term in Eq. (14) can be further decomposed into two terms:  $u_x\omega_y$  and  $-u_y\omega_x$ . The first term represents the contribution of the spanwise vorticity (mainly the LEVs) to the total lift. The second term represents the contribution of the streamwise vorticity (mainly the TVs or the SEVs). From Figure 15, it is apparent that the lift generation is always dominated by the  $u_x\omega_y$  term, in the plates with or without oscillation. Thus, the LEV is always the main contributor to the lift generation, and the lift enhancement in a spanwise oscillating plate is primarily caused by the modulation of the LEV (which corresponds to the change in the  $u_x\omega_y$  term). From Figures 5 and 7, we find that the lift-enhancement effect of the spanwise oscillation is more significant at intermediate or high angles of attack. This is because the LEV strength becomes too weak at very low angles of attack ( $\alpha < 15^\circ$ ). Note that although the spanwise oscillation produces a large spanwise velocity, the lift-enhancement effect due to the change in the  $-u_y\omega_x$  term is quite limited.

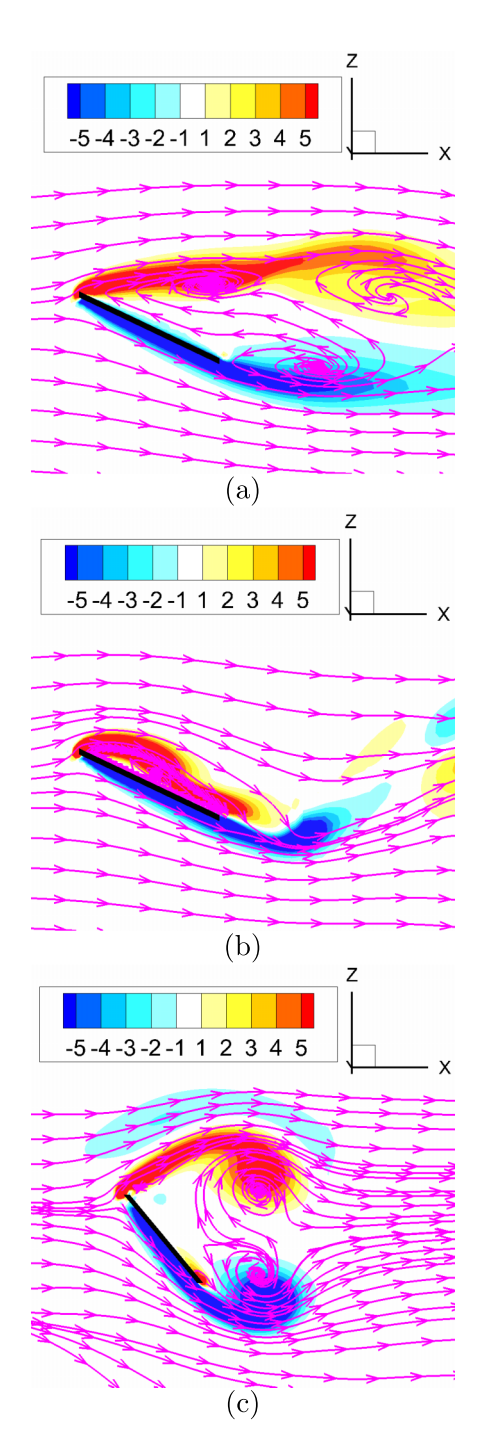


FIG. 14. The streamlines and spanwise vorticity contours on the mid-span slice when the lift coefficient reaches its maxima for a flat-plate (AR = 2.0, Re = 300, and  $\alpha = 25^{\circ}$ ) (a) in purely forward flight and (b) in forward flight with the spanwise oscillation of k = 0.5 and  $A_y = 1.0$ . (c) The streamlines and spanwise vorticity contours on the mid-span slice when the lift coefficient reaches its maxima for a flat-plate in hovering flapping flight (in the validation case presented in Sec. II A). Please note that in (c) we use a coordinate-system which moves with the instantaneous translational velocity of the flapping foil.

The distorted LEVs shown in Figure 13 resemble (to some extent) the conical, spiral vortices which appear on the upper surface of a delta-wing. For a delta-wing, it has long been recognized that the spanwise velocity component is essential for the stability of the LEVs.<sup>26</sup> The spanwise velocity component can facilitate the transportation of vorticity out to the wing-tip and thus prevent

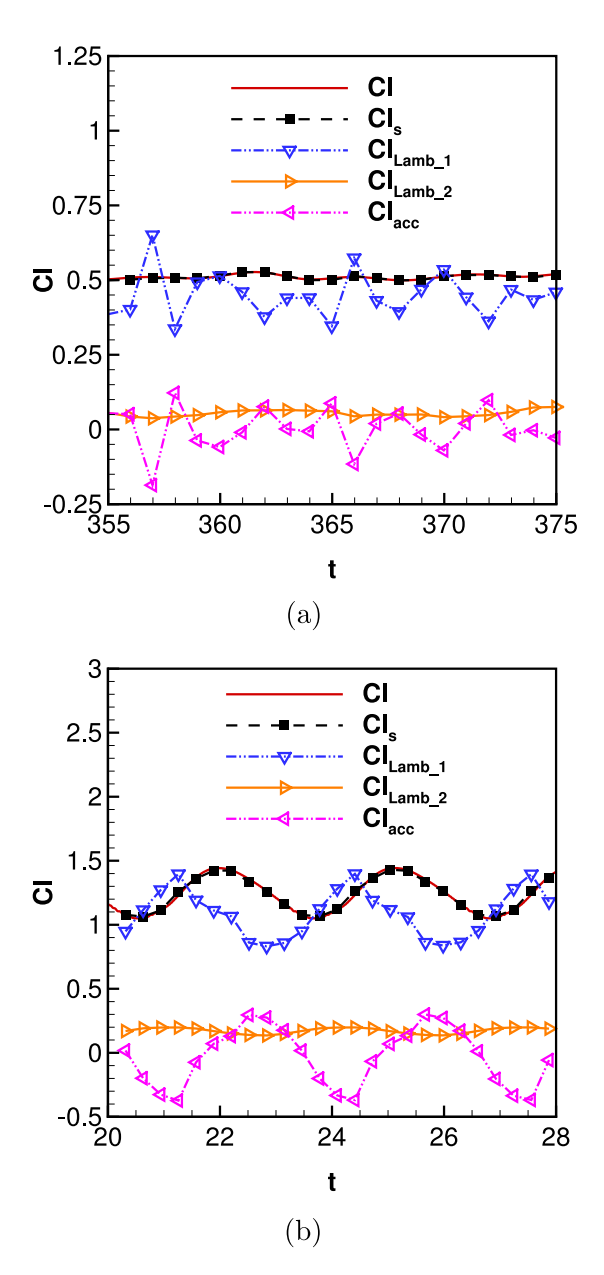


FIG. 15. A breakdown of the lift coefficients using the simplified lift formula for flat-plates (AR = 2.0, Re = 300, and  $\alpha = 25^{\circ}$ ) (a) without oscillation and (b) with the spanwise oscillation of k = 0.5 and  $A_y = 1.0$ . Cl and  $Cl_s$  denote the lift coefficients obtained using the Lagrangian forces (Eq. (6)) and the simplified lift formula (Eq. (14)), respectively.

the LEV from accumulating into a large unstable vortex. The similarity between the stability of the LEVs in insects' flapping wings and that of the LEVs in the delta-wings has been addressed previously in some references. 1.27 However, the role of the spanwise flow in stabilizing the LEVs in the flapping flights of animals is still controversial. Birch and Dickinson<sup>28</sup> proposed that the stabilization of LEV was due to the downwash induced by the tip vortex. Lentink and Dickinson<sup>29</sup> showed that the LEV can be stabilized by the centripetal and Coriolis accelerations.

We conjecture that the stabilization mechanism of the LEVs in the spanwise oscillating plates also shares the similarity with that of the LEVs in delta-wings. Here, we use  $\left|-(u_y - \dot{Y})\partial \omega_y/\partial y\right|$  (where  $\dot{Y}$  is the spanwise oscillating velocity of the flat-plate) to quantify the strength of vorticity transport in the spanwise direction. <sup>18</sup> In Figure 16, we compare the spanwise vorticity transport in a flat-plate in forward flight, a flat-plate in forward flight with spanwise oscillation, and a flat-plate

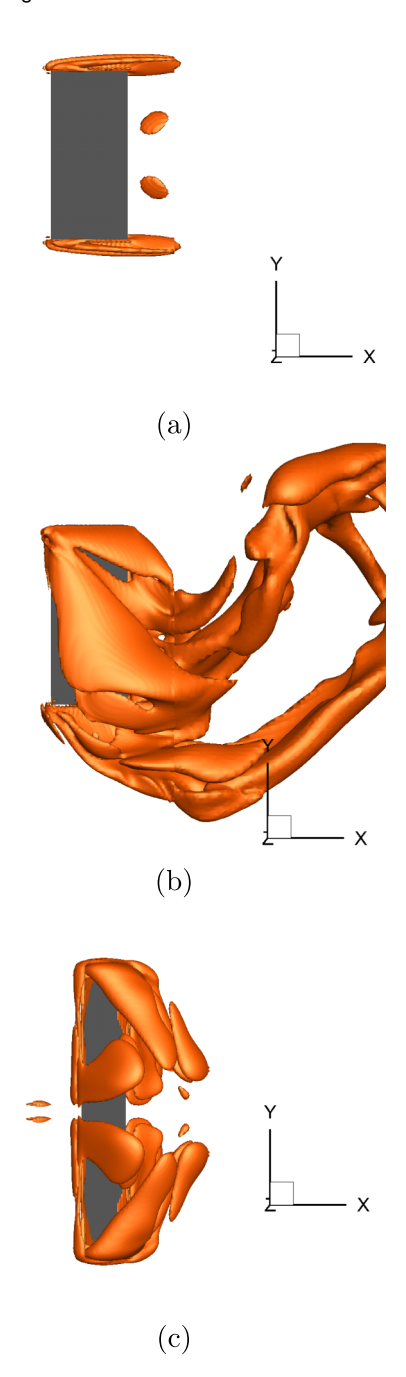


FIG. 16. The transport of spanwise vorticity at the moment when the lift coefficient reaches its maxima for a flat-plate  $(AR = 2.0, Re = 300, \text{ and } \alpha = 25^{\circ})$  (a) in purely forward flight and (b) in forward flight with the spanwise oscillation of k = 0.5 and  $A_y = 1.0$ . (c) The transport of spanwise vorticity at the moment when the lift coefficient reaches its maxima for a hovering flapping flat-plate (in the validation case presented in Sec. II A). The iso-surfaces for  $\left|-(u_y - \dot{Y})\partial\omega_y/\partial y\right| = 2.0$  are shown, with  $\dot{Y}$  being zero for (a) and (c).

in hovering flapping flight (the validation case presented in Sec. II B). It is seen that in the case of spanwise oscillating plate, the spanwise vorticity transport is greatly enhanced, if compared with the case of purely forward flight. For the hovering flapping plate, the enhanced spanwise vorticity transport is also evident. It should be noted that despite the similarity in the stabilization mechanism of LEVs, the origins of the spanwise velocity component in different scenarios aforementioned are very different. For the delta-wings, the spanwise velocity component is induced by the geometric backswept. For the spanwise oscillating plates, the spanwise velocity component is directly brought

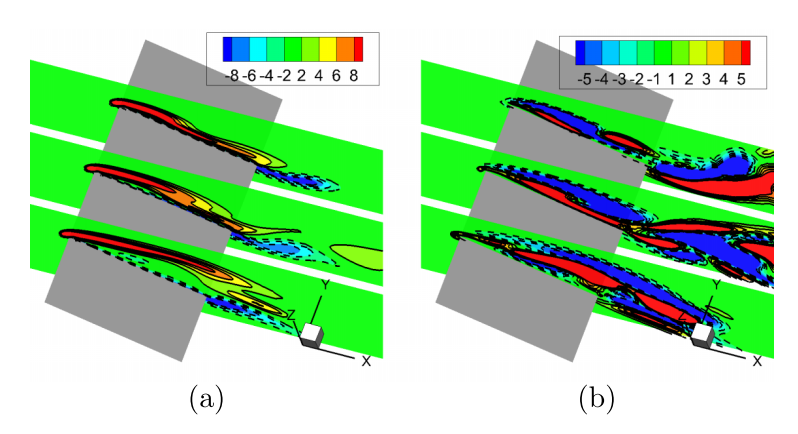


FIG. 17. The contours of spanwise vorticity and spanwise vorticity transport  $(-(u_y - \dot{Y})\partial\omega_y/\partial y)$  at three different slices (25%, 50%, and 75% span) when the lift coefficient reaches its maxima for a spanwise oscillating plate (AR = 2.0, Re = 300,  $\alpha = 25^\circ$ , k = 0.5, and  $A_y = 1.0$ ): (a) spanwise vorticity contours; (b) spanwise vorticity transport contours.

about by the prescribed kinematics. For the flapping plates, the origin of the spanwise velocity component is a complex problem which is beyond the scope of this work.

In Figure 17, we show the contours of the spanwise vorticity transport term,  $-(u_y - \dot{Y})\partial\omega_y/\partial y$ , for the oscillating plate at three different slices along the span (corresponding to Figure 16(b)). For the purpose of reference, the contours of the spanwise vorticity on these three slices are also shown. It is clearly seen that the spanwise vorticity transport becomes intensive at the LEV core. This finding is consistent with that in Wong and Rival, <sup>30</sup> where the spanwise vorticity transport was found to improve LEV stability by acting as a sink for vorticity generated in the leading edge shear layer.

The LEV stabilization mechanism associated with the spanwise vorticity transport can also be used to explain why the high-frequency oscillations (with low-amplitudes) are not efficient in boosting the aerodynamic performance (please see the relevant discussion in Figure 9 of Sec. III A). In the case of high-frequency oscillations, although a spanwise flow can be induced, the accumulated vorticity does not have enough time to be transported laterally before the spanwise flow reverses its direction.

#### IV. CONCLUSIONS

We numerically investigate the aerodynamic performance of low-aspect-ratio flat-plates with harmonic spanwise oscillations in low-Reynolds number flows. There are five control parameters in this problem: the Reynolds number Re, the aspect ratio AR, the angle of attack  $\alpha$ , the reduced frequency k, and the dimensionless amplitude  $A_y$ . In this work, the Reynolds number Re is fixed to 300 and the effects of other parameters on the aerodynamic performance are studied.

In a certain range of the parameter space  $(k, A_y)$ , it is found that the spanwise oscillation can significantly enhance the time-averaged lift coefficient and augment the time-averaged lift-to-drag ratio. The enhancement of lift is found to be more effective for post-stall flows at intermediate and high angles of attack. Among all cases, the optimal power efficiency for lift-generation is achieved by oscillations with moderate strength. It is also found that the lift-enhancement effect of spanwise oscillation is not very sensitive to the variation of aspect ratios (in the range of  $1 \le AR \le 3$ ).

The enhancement of lift in the spanwise oscillating plates is attributable to the presence of LEVs at a place very close to the upper surface. The effect of the modulated vortical structures on lift production is further quantified by using a simplified lift formula which links the lift with the Lamb vector term. The imposed spanwise oscillation is found to enhance the vorticity transport along the spanwise direction, which in turn stabilizes the LEVs on the flat-plate. The results of this work shed some new light on the counterintuitive high-lift in the gliding flights of tree snakes.

#### **ACKNOWLEDGMENTS**

We would like to thank Professor Tianshu Liu at Western Michigan University for valuable discussions regarding the lift enhancement mechanism. This work was supported by National Natural Science Foundation of China (Grant Nos. 11372331, 11302238, 11232011, 11021262, and 11023001) and the National Basic Research Program of China (Grant No. 2013CB834100). The authors would like to thank the National Supercomputing Center in Tianjin (NSCC-TJ) for the allocation of computing time.

- <sup>1</sup> C. P. Ellington, C. V. D. Berg, A. P. Willmott, and A. L. R. Thomas, "Leading-edge vortices in insect flight," Nature 384, 626–630 (1996).
- <sup>2</sup> H. Liu, C. P. Ellington, K. Kawachi, C. V. D. Berg, and A. P. Willmott, "A computational fluid dynamic study of hawkmoth hovering," J. Exp. Biol. **201**, 461–477 (1998).
- <sup>3</sup> J. H. Wu and M. Sun, "Unsteady aerodynamic forces of a flapping wing," J. Exp. Biol. 207, 1137–1150 (2004).
- <sup>4</sup> W. Shyy and H. Liu, "Flapping wings and aerodynamic lift: The role of leading-edge vortices," AIAA J. 45, 2817–2819 (2007).
- <sup>5</sup> D. Lentink, W. B. Dickson, J. L. V. Leeuwen, and M. H. Dickinson, "Leading-edge vortices elevate lift of autorotating plant seeds," Science **324**, 1438–1440 (2009).
- <sup>6</sup> T. Y. Hubel, N. I. Hristov, S. M. Swartz, and K. S. Breuer, "Time-resolved wake structure and kinematics of bat flight," Exp. Fluids **46**, 933–943 (2009).
- <sup>7</sup> K. Viswanath, K. Nagendra, J. Cotter, M. Frauenthal, and D. K. Tafti, "Straight-line climbing flight aerodynamics of a fruit bat," Phys. Fluids 26, 021901 (2014).
- <sup>8</sup> K. Viswanath, K. Nagendra, and D. K. Tafti, "Climbing flight of a fruit bat deconstructed," AIAA Paper 2014-0220, 2014.
- <sup>9</sup> S. Z. Wang, X. Zhang, G. W. He, and T. S. Liu, "Lift enhancement by stretching and retracting wingspan in flapping flight," Phys. Fluids 26, 061903 (2014).
- <sup>10</sup> J. J. Socha, "Gliding flight in the paradise tree snake," Nature **418**, 603–604 (2002).
- <sup>11</sup> J. J. Socha, "Gliding flight in chrysopelea: Turning a snake into a wing," Integr. Comp. Biol. 51, 969–982 (2011).
- <sup>12</sup> K. Miklasz, M. Labarbera, X. Chen, and J. Socha, "Effects of body cross-sectional shape on flying snake aerodynamics," Exp. Mech. 50, 1335–1348 (2010).
- <sup>13</sup> D. Holden, J. J. Socha, N. Cardwell, and P. P. Vlachos, "Aerodynamics of the flying snake chrysopelea paradisi: How a bluff body cross-sectional shape contributes to gliding performance," J. Exp. Biol. 217, 382–394 (2014).
- <sup>14</sup> A. Krishnan, J. J. Socha, P. P. Vlachos, and L. A. Barba, "Lift and wakes of flying snakes," Phys. Fluids 26, 031901 (2014).
- <sup>15</sup> S. Z. Wang and X. Zhang, "An immersed boundary method based on discrete stream function formulation for two- and three-dimensional incompressible flows," J. Comput. Phys. 230, 3479–3499 (2011).
- <sup>16</sup> R. Mittal, H. Dong, M. Bozkurttas, F. Najjar, A. Vargas, and A. von Loebbecke, "A versatile sharp interface immersed boundary method for incompressible flows with complex boundaries," J. Comput. Phys. 227, 4825–4852 (2008).
- <sup>17</sup> S. Z. Wang, G. W. He, and X. Zhang, "Parallel computing strategy for a flow solver based on immersed boundary method and discrete stream-function formulation," Comput. Fluids 88, 210–224 (2013).
- <sup>18</sup> K. Taira and T. Colonius, "Three-dimensional flows around low-aspect-ratio flat-plate wings at low Reynolds numbers," J. Fluid Mech. 623, 187–207 (2009).
- 19 W. Shyy, P. Trizila, C. Kang, and H. Aono, "Can tip vortices enhance lift of a flapping wing?," AIAA J. 47, 289–293 (2009).
- <sup>20</sup> J. J. Socha, T. O'Dempsey, and M. LaBarbera, "A 3-d kinematic analysis of gliding in a flying snake, *Chrysopelea paradisi*," J. Exp. Biol. 208, 1817–1833 (2005).
- <sup>21</sup> Z. J. Wang, "Two dimensional mechanism for insect hovering," Phys. Rev. Lett. **85**, 2216–2219 (2000).
- <sup>22</sup> J. H. J. Buchholz and A. J. Smits, "The wake structure and thrust performance of a rigid low-aspect-ratio pitching panel," J. Fluid Mech. 603, 331–365 (2008).
- <sup>23</sup> Z. J. Wang, "Aerodynamic efficiency of flapping flight: Analysis of two-stroke model," J. Exp. Biol. 211, 234–238 (2008).
- <sup>24</sup> D. Lentink, S. R. Jongerius, and N. L. Bradshaw, "The scalable design of flapping micro air vehicles inspired by insect flight," in *Flying Insects and Robots*, edited by D. Floreano, J. C. Zufferey, M. V. Srinivasan, and C. Ellington (Springer, Berlin, Hamburg, 2009).
- <sup>25</sup> S. Z. Wang, X. Zhang, G. W. He, and T. S. Liu, "A lift formula applied to low-Reynolds-number unsteady flows," Phys. Fluids 25, 093605 (2013).
- <sup>26</sup> J. Z. Wu, A. D. Vakili, and J. M. Wu, "Review of the physics of enhancing vortex lift by unsteady excitation," Prog. Aerosp. Sci. 28, 73–131 (1991).
- <sup>27</sup> C. V. dan Berg and C. P. Ellington, "The three-dimensional leading-edge vortex of a 'hovering' model hawkmoth," Philos. Trans. R. Soc. London, Ser. B 352, 329–340 (1997).
- <sup>28</sup> J. M. Birch and M. H. Dickinson, "Spanwise flow and the attachment of the leading-edge vortex on insect wings," Nature 412, 729–733 (2001).
- <sup>29</sup> D. Lentink and M. H. Dickinson, "Rotational accelerations stabilize leading edge vortices on revolving fly wings," J. Exp. Biol. 212, 2705–2719 (2009).
- <sup>30</sup> J. G. Wong and D. E. Rival, "Determining the relative stability of leading-edge vortices on nominally two-dimensional flapping profiles," J. Fluid Mech. 766, 611–625 (2015).